JACS
JOURNAL OF THE AMERICAN CHEMICAL SOCIETY
Article
Cite This: J. Am. Chem. Soc. 2018, 140, 1900−1909
pubs.acs.org/JACS

Orbital Control of Photocurrents in Large Area All-Carbon Molecular Junctions

Amin Morteza Najarian,[†,‡] Akhtar Bayat,[†,‡] and Richard L. McCreery*[,†,‡]

[†]Department of Chemistry, University of Alberta, Edmonton, Alberta, Canada, T6G 2R3
[‡]National Institute for Nanotechnology, National Research Council Canada, Edmonton, Alberta, Canada, T6G 2G2

Supporting Information

ABSTRACT: Photocurrents generated by illumination of carbon-based molecular junctions were investigated as diagnostics of how molecular structure and orbital energies control electronic behavior. Oligomers of eight aromatic molecules covalently bonded to an electron-beam deposited carbon surface were formed by electrochemical reduction of diazonium reagents, with layer thicknesses in the range of 5−12 nm. Illumination through either the top or bottom partially transparent electrodes produced both an open circuit potential (OCP) and a photocurrent (PC), and the polarity and spectrum of the photocurrent depended directly on the relative positions of the frontier orbitals and the electrode Fermi level (E_F). Electron donors with relatively high HOMO energies yielded positive OCP and PC, and electron acceptors with LUMO energies closer to E_F than the HOMO energy produced negative OCP and PC. In all cases, the PC spectrum and the absorption spectrum of the oligomer in the molecular junction had very similar shapes and wavelength maxima. Asymmetry of electronic coupling at the top and bottom electrodes due to differences in bonding and contact area cause an internal potential gradient which controls PC and OCP polarities. The results provide a direct indication of which orbital energies are closest to E_F and also indicate that transport in molecular junctions thicker than 5 nm is controlled by the difference in energy of the HOMO and LUMO orbitals.

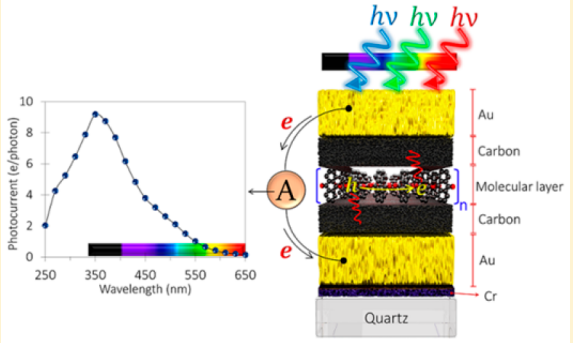

INTRODUCTION

Molecular electronics (ME) refers to a research area pursuing the idea of using single molecules or layers of molecules as nanoscale functional building blocks in electronic devices.[1−5] ME has resulted in reported devices capable of handling a variety of electronic functions, including nonlinear resistance,[6,7] rectification,[8−11] memory,[12−14] and conductance switching.[15,16] Recent advances in measurement capabilities and fabrication techniques have enabled researchers to push the frontiers of ME beyond the investigation of charge transport to broader aspects of spintronics,[17,18] plasmonics,[19−21] optoelectronics,[22,23] and thermoelectric effects.[24,25] Molecular optoelectronics is an interdisciplinary research area that studies the interaction of light with the functioning molecular junction (MJ).[26] Apart from novel and potentially important applications, optoelectronic measurements can provide a direct and valuable diagnostic of electron transfer mechanism and energy level alignment of molecular layers in contact with electrodes in "molecular junctions (MJ)".[3,26] Detailed understanding of how molecular structure affects the energy landscape, and charge transport in molecular devices is a core aspiration of molecular electronics, which should enable rational design of the molecular devices for the functions and characteristics which are difficult or impossible with conventional semiconductors.

Photocurrents generated by internal photoemission (IPE) have been used to probe energy barriers in classical inorganic tunnel junctions,[27−32] semiconductor/molecule devices,[33] and more recently molecular electronics.[34,35] The minimum photon energy required to generate a photocurrent (PC) is directly related to internal energy barriers, often the offsets between the contact Fermi levels and the highest occupied molecular orbital (HOMO) or lowest unoccupied molecular orbital (LUMO), depending on the molecule involved. The PCs observed in thin molecular junctions (thickness, d < 4 nm) with copper as a partially transparent top contact are consistent with the IPE mechanism, provided the photon energy is in a region where light absorption by direct HOMO−LUMO (H−L) transitions in the molecule are insignificant.[34,35] The energy barriers observed with IPE on carbon/molecule/Cu MJs are similar to those measured by Ultraviolet Photoelectron Spectroscopy, and are consistent with transport measurements of similar MJs.[34−36] However, charge transport in carbon/molecule/Cu MJs with d < 5 nm is weakly dependent on variations in molecular structure for aromatic molecules due to the strong electronic coupling between the molecular layer and the contacts.[36−38] Such coupling results in realignments of energy levels in the molecules from those of the isolated molecules, thus reducing the influence of orbital energies on transport barrier height.

Received: December 1, 2017
Published: January 10, 2018

DOI: 10.1021/jacs.7b12577
J. Am. Chem. Soc. 2018, 140, 1900−1909

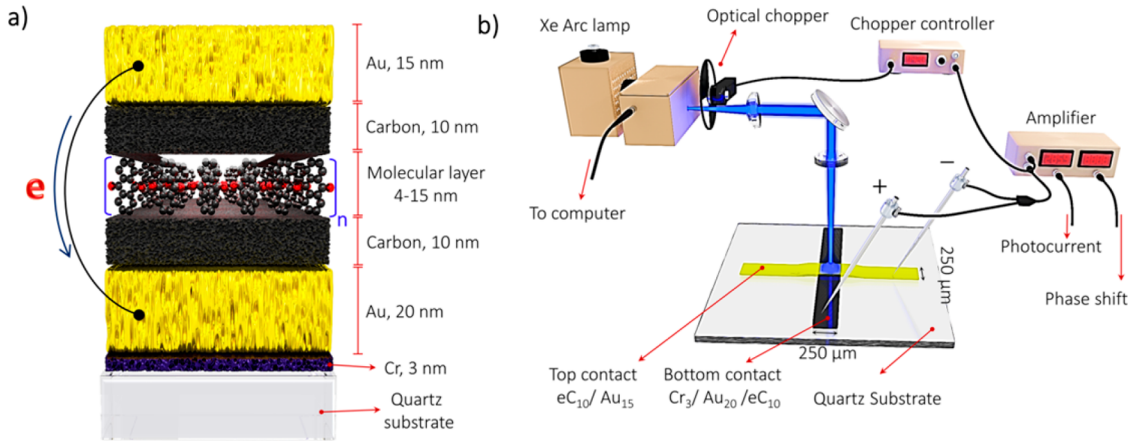

Figure 1. Structure of the molecular junction and photocurrent apparatus. (a) Schematic illustration of Quartz/Cr_3/Au_{20}/eC_{10}/Anthraquinone/eC_{10}/Au_{15} molecular junction. *n* is a number of repeating units of the oligomer which determine final thickness of the molecular layer. Arrow at left indicates the direction of electron flow in the external circuit corresponding to positive PC polarity. (b) Apparatus used for the PC measurement with continuum source, modulation by an optical chopper, and detection with a lock-in amplifier. Phase shifts near 0° indicate positive PC polarity while those near 180° indicate negative PC.

Several reports have appeared on changes in transport behavior when the molecular layer thickness exceeds 4−5 nm, some of which are attributed to a change in mechanism from coherent tunneling to an alternative "hopping" mechanism.[39,40] Recently, we showed that transport beyond 5 nm in carbon-based aromatic molecular junctions is controlled by the structure and orbital energies of the molecular layer.[6] We proposed multistep tunneling as a dominant transport mechanism, with a barrier determined by the H−L gap, and not by the charge injection barrier at the molecule/electrode interface. While coherent transport (single step tunneling) is not expected for distances longer than 4−5 nm, PCs provide a potentially informative probe of internal energy levels in completed MJs, in order to elucidate how molecular structure affects transport.

We report herein an investigation of the origins of the PC response in large area carbon-based MJs with d > 5 nm and a variety of molecular structures. The "all-carbon" MJ structure consisting of covalently bonded oligomers between electron-beam deposited carbon electrodes provided contacts with equal work functions and sufficient optical transparency to permit light transmission through the entire, functioning molecular junction. If the incident photon energy is within the optical absorption band of the molecule, the electronic response differs fundamentally from IPE, in which photon absorption occurs in the electrodes and is followed by transport of the excited electron across an energy barrier. We demonstrate that both the H−L gap in the molecular layer and the energy offset of the frontier molecular orbitals relative to the electrode Fermi energy (E_F) affect the PC, such that unequivocal assignment of the carrier sign becomes possible. The results are consistent with multistep tunneling through the H−L gaps when the molecular layer is thicker than 5 nm. Not only do PCs provide a diagnostic of device properties and transport mechanisms, but the results are also relevant to the rational design of molecular electronic devices with unusual electronic behaviors.

RESULTS

Molecular Junction Fabrication. Large area molecular junctions were fabricated by established procedures[41] on electron-beam deposited carbon (eC) surfaces with a covalently bonded molecular layer thicker than 4 nm. eC is a form of amorphous conducting carbon with 30−40% sp^3 hybridized carbon and the remainder sp^2 carbon.[41] Figure 1a shows a cross section of a completed junction on a quartz substrate. The bottom contact is made by successive electron-beam deposition of Cr, Au, and eC. Combining the adhesion ability of the deposited Cr layer and the high conductivity of Au thin film with the flatness and surface chemistry of eC makes an ideal electrode with demonstrated high stability and yields for MJ fabrication.[41] Molecular layers were covalently grafted on the surface of eC by electrochemical reduction of diazonium reagents in acetonitrile. The thickness of the molecular layer was controlled by the electrochemical parameters listed in Supporting Information section 1 and was verified by AFM "scratching".[36] Deposition of eC and Au as the top contact completes the molecular junction, designated Cr_3/Au_{20}/eC_{10}/$NAB_{6.0}$/eC_{10}/Au_{15} (subscripts indicate layer thicknesses, and NAB = nitro-azobenzene oligomer in this example). Detailed fabrication steps are provided in the Methods section and Supporting Information section 1.

Photocurrent Measurements. The schematic of the optical apparatus and PC measurement is shown in Figure 1b, with the molecular junction maintained at zero bias unless noted otherwise. A Xe arc source passed through a monochromator ($\Delta\lambda$ = 13 nm) and then an optical chopper before being focused on the sample. The 250 × 250 μm^2 molecular junction was centered in the focal spot, which had a diameter of ∼2 mm. The AC PC phase and amplitude were monitored by a lock-in amplifier referenced to the chopping frequency while the wavelength was scanned by the monochromator. The PC polarity was determined by calibrating the phase shift output of the lock-in amplifier with a silicon photocell as the sample. A near-zero phase angle indicates a positive PC with electrons flowing from the top to bottom contacts in the external circuit, while a phase near 180° indicates negative PC. Laser illumination with DC current measurement was used for further validation of the PC sign for each of the eight molecular junction structures examined. In order to determine the external quantum efficiency (EQE), the incident optical power on the junction at each wavelength was measured by a Newport power meter. The light power density

DOI: 10.1021/jacs.7b12577
J. Am. Chem. Soc. 2018, 140, 1900−1909

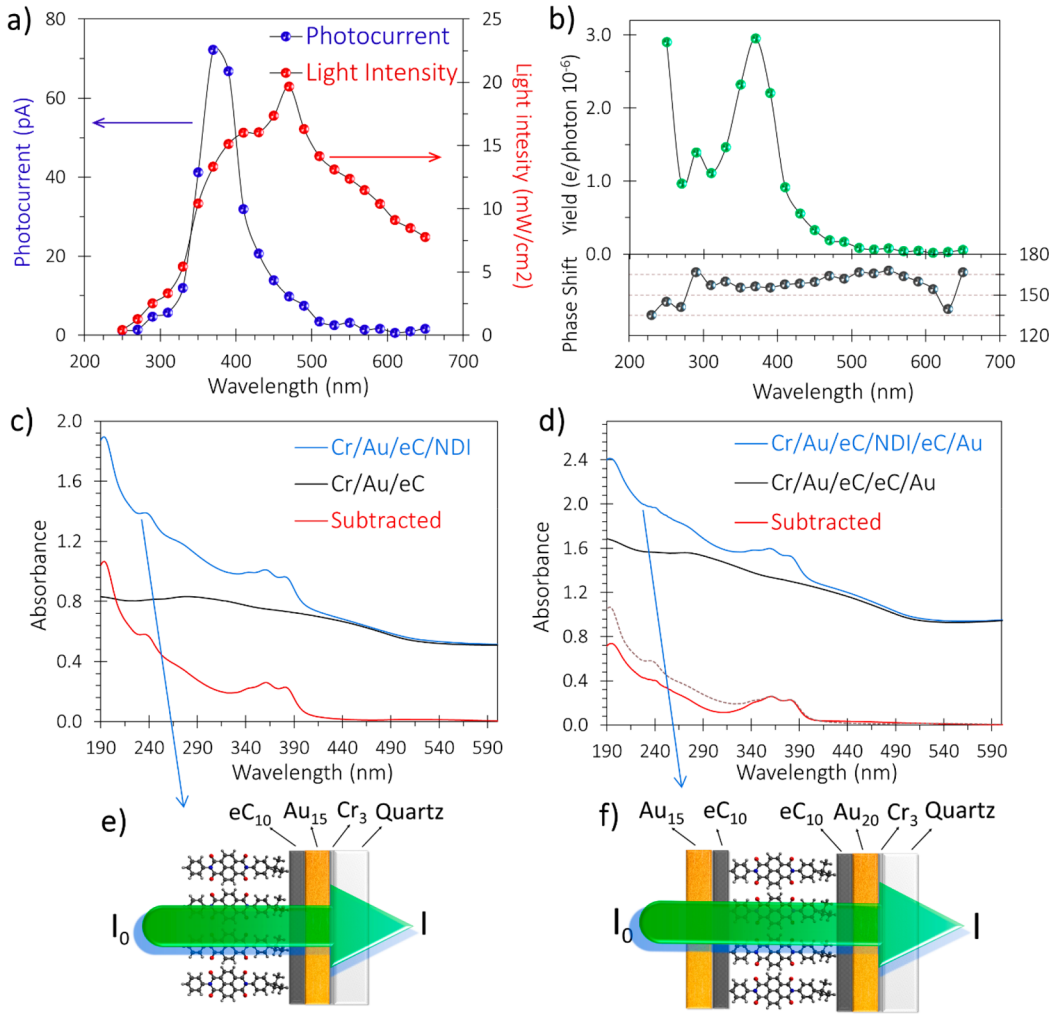

Figure 2. Determination of external quantum efficiency and UV−vis absorption of molecular layers and complete MJs. (a) Overlay of Photocurrent spectrum for NDI MJ and illuminated light intensity of Xe arc lamp measured at the sample. (b) Corresponding PC yield and phase shift spectra for the NDI results shown in panel (a). (c) Overlay of optical absorbance of Quartz/Cr_3/Au_{20}/eC_{10} (black curve) and the same electrode after NDI grafting on the surface (blue curve). Red curve is the NDI spectrum after subtraction of the substrate spectrum. (d) Overlay of absorbance spectrum of "blank" Quartz/Cr_3/Au_{20}/eC_{10}/eC_{10}/Au_{15} MJ (black curve) and complete junction *viz* Quartz/Cr_3/Au_{20}/eC_{10}/NDI/eC_{10}/Au_{15} (blue curve). Red curve is the complete MJ spectrum minus the "blank", with dashed curve repeated from panel (c). (e) Schematic of the bottom contact electrode structure modified with NDI molecular layer. (f) Schematic of the complete NDI MJ including top contact.

varied with wavelength as shown in Figure 2a, equaling 0.34 to 21.8 mW/cm^2 over the wavelength range of 250 to 650 nm. PCs were measured over the same range of wavelengths to determine junction EQE at each photon energy. As an example, the observed PC of a phenyl naphthalene di-imide (NDI) molecular junction is shown in Figure 2a. By combining the source output spectrum with the PC response as functions of wavelength, the yield or EQE as photoelectrons/incident photon was determined and plotted in Figure 2b (calculation details appear in Supporting Information section 2). The corresponding phase shift is also shown in Figure 2b; the ~150° phase across the entire wavelength range indicates a negative PC, with electrons traveling from the bottom to the top contact in the external circuit.

UV−vis Absorption. The partial transparency of the eC/Au contacts permits UV−vis absorption spectroscopy of both the Au/eC/oligomer surface and the completed molecular junction. In situ absorbance spectra provide direct indications of changes and broadening of molecular orbital energies in the local environment of completed, functioning MJ, and permit correlations with observed PCs (below). Figure 2c shows absorbance spectra (relative to air) of a 1.8 × 1.2 cm^2 blanket Q/Cr_4/Au_{20}/eC_{10} electrode, compared to the same electrode after electrochemical grafting of an NDI molecular multilayer. Subtraction of these two spectra clearly shows the absorbance of multilayer NDI molecules that are covalently grafted and grown on the surface of eC (red line). Figure 2d shows the absorbance of the completed junction after deposition of the top contact on the same device shown in panel c. Subtraction of the completed junction from the same electrode structure without molecular layer grafting (Q/Cr_4/Au_{20}/eC_{10}/eC_{10}/Au_{15}) reveals the absorbance of the NDI molecular layer in the transport environment (red line).

Correlation of Photocurrent with Absorbance. When the molecules are covalently grafted on the eC surface and undergo oligomer formation, the energy levels of the molecules could significantly change from those of the isolated molecule. Intra- and interchain interactions, and more importantly electronic coupling with contacts, are among the reasons for changes in energy levels in the solid state compared to the free

DOI: 10.1021/jacs.7b12577
J. Am. Chem. Soc. 2018, 140, 1900−1909

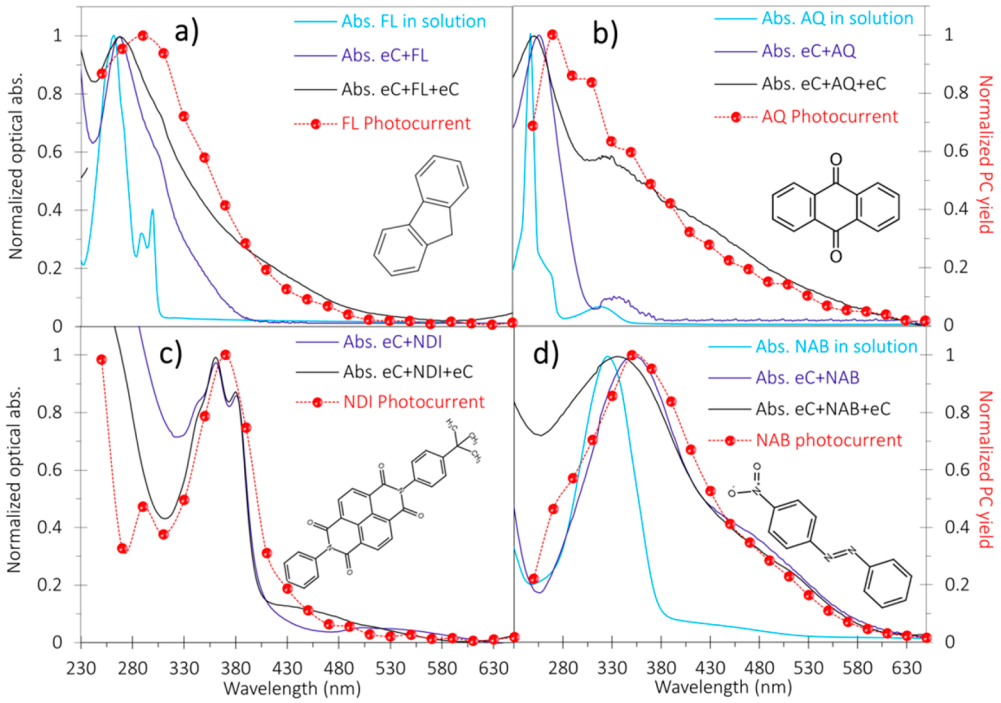

Figure 3. Overlay of PC yield and absorption spectra for four molecules: (a) FL, (b) AQ, (c) NDI, (d) NAB. Absorption spectra of each molecule in different media are shown: (i) isolated monomer in solution (blue lines); (ii) multilayer grafted on the surface of bottom contact (purple lines); (iii) multilayer grafted on the surface in complete junction including top contact (black lines). All spectra are corrected for the blank electrode absorption as shown in Figure 2 and normalized to the maximum peak of 1.0. PC spectra (red lines) are shown in the secondary axis at the right side of the graphs with positive sign regardless of the actual measured polarity. See also Figures S5–S12 for TD-DFT prediction of absorption spectra and MO visualization of tested molecules.

Table 1. Summary of Photocurrent Results and DFT Predicted Energy Levels of Examined Molecules

molecules	φ_h (eV)[a] ($E_F - E_{HOMO}$)	φ_e (eV)[a] ($E_{LUMO} - E_F$)	smaller barrier	OCP sign at 407 nm	photocurrent sign[b]	max of photocurrent (eV)	max of Abs (eV)[c]	max of TD-DFT (eV)[d]
AN	0.42	3.17	ϕ_h	+	+	4.28	N/A	3.26
BTB	0.69	3.32	ϕ_h	+	+	3.35	3.46	3.54
FL	1.14	4.09	ϕ_h	+	+	4.28	4.62	4.75
TB	1.42	3.47	ϕ_h	+	+	3.76	4.24	4.44
NDI	2.32	1.45	ϕ_e	−	−	3.35	3.42	3.40
NAB	2.05	1.76	ϕ_e	−	−	3.54	3.56	3.49
AQ	2.40	2.01	ϕ_e	−	−	4.28	4.84	5.10
NP	2.99	2.37	ϕ_e	−	−	3.35	N/A	4.88

[a]Fermi level of eC measured by UPS at −4.8 eV.[41] [b]The PC sign over the entire wavelength range observed. [c]The absorbance of the molecule grafted on eC, after subtraction of eC spectrum. [d]All DFT calculations were performed on free molecules with Gaussian 09 using B3LYP 6-31G(d).

molecules. We used the UV–vis absorption spectrum to identify the wavelengths of maximum absorption in the complete junction, and to observe changes in orbital energies. Figure 3 shows the optical absorbance of four molecules in different media: (i) dilute acetonitrile solution (blue lines), (ii) multilayer grafted on the surface of eC (purple lines), (iii) multilayer between two contacts in the full stack of the junction (black lines). In the two latter cases, the spectra of unmodified electrodes were subtracted to reveal the molecular layer spectrum, as shown in Figure 2c and 2d for NDI. In all cases, bonding to eC and application of the top contact has minor effects (<18 nm) on the peak absorption wavelength, implying that the optical gap of the molecule is not strongly affected by the contacts and multilayer formation. However, there is a significant red shift in absorption onset for AQ, FL, and NAB upon bonding to eC, and a further red shift upon deposition of the top contact. We previously discussed the possible causes for these observations and concluded that they are due to strong coupling between the aromatic molecular layer and the contacts,[6] and are responsible for the small effects of the molecular structure when d < 5 nm.[36] However, the minor changes in the UV–vis spectrum with increasing layer thickness implies relative weak coupling between molecular subunits, and a limited conjugation length within the interior layer.[6] The main question in the current report is a correlation of the absorption and PC spectra, to determine the origin of PC generation. Figure 3 shows overlays of the absorption and PC spectra for FL, AQ, NAB, and NDI, and additional examples are provided in Figures S5–S12. The absorbance and PC spectra are normalized to a maximum value of 1.0 to permit direct comparison of spectrum shapes and maximum wavelengths. Note first that the PCs are negligible at wavelengths where the molecular layer does not absorb significantly for eight different molecular layers, all with d > 4 nm; the PC

DOI: 10.1021/jacs.7b12577
J. Am. Chem. Soc. 2018, 140, 1900–1909

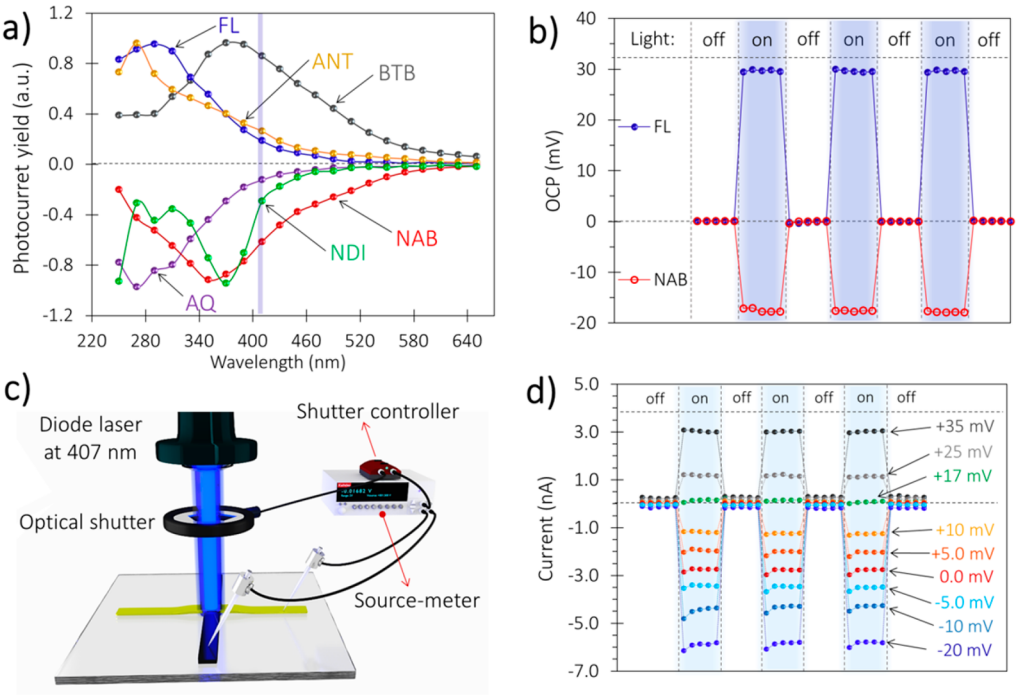

Figure 4. Polarity of the photocurrent and OCP measurement. (a) Overlay of the PC yield for six indicated molecules, with the sign of the yield indicating PC polarity. Maximum PC yield normalized to ±1.0 for comparison. (b) Observed OCP for three on/off light cycles for FL and NAB MJs. (c) Schematic of OCP apparatus. Keithley 6517 is used as the source-meter for OCP measurement. (d) Observed current for light on/off cycles with the indicated bias applied to a NAB MJ. Dark current is not subtracted; however, it is much smaller than the PC.

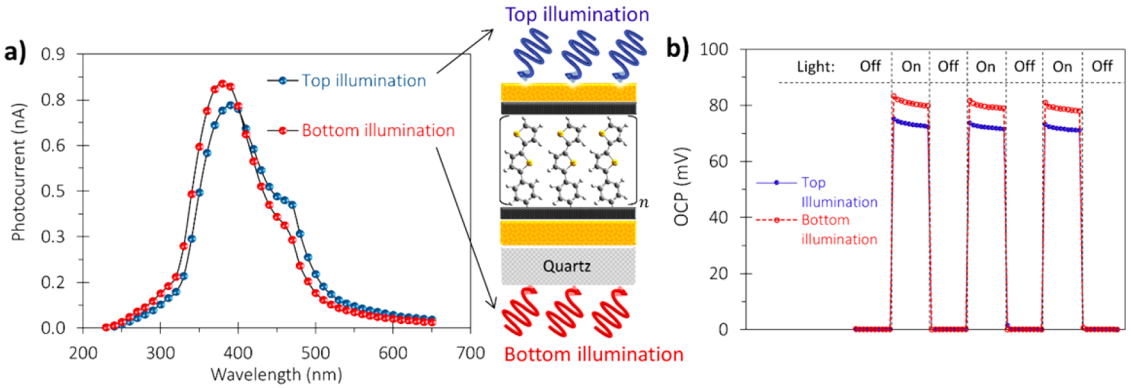

Figure 5. (a) Observed PC for "top" and "bottom" illumination of a BTB MJ by the Xe arc source, using the same electronic conditions as Figure 4a. (b) Observed OCP for three on/off light cycles for BTB MJ with top and bottom illumination by a 407 nm diode laser.

response tracks the absorbance of the molecules, as modified by interactions with the contacts. The maximum wavelengths and polarities of the PC and absorbance spectra are summarized in Table 1.

Open-Circuit Potential and Photocurrent Polarity. Figure 4a compares the PCs of the four molecules in Figure 3 plus bis-thienyl-benzene (BTB) and anthracene (AN), plotted to indicate the PC polarity. FL, AN, and BTB are consistently positive provided $d > 4$ nm, while AQ, NDI, and NAB are consistently negative. Note that the PC sign and phase are independent of the thickness of the molecular layer for the relatively thick MJs examined ($d > 4$ nm). As shown in Figure S13 for the examples of FL and AQ, the PC magnitudes vary with molecular layer thickness, but polarity and maximum wavelength remain constant over all thicknesses examined. To further confirm the PC sign, we monitored the open circuit potential (OCP) during DC illumination by a 6 mW, 407 nm diode laser, which could be interrupted by a mechanical aperture, as shown in Figure 4c. Figure 4b shows the OCP of FL and NAB junctions during several laser exposures lasting ~5 s each. The significant, sign selective, and reversible photovoltage generation upon exposure to laser radiation indicates that there is a light-induced electric field in the MJ, in which the negative sign of OCP implies that the bottom contact becomes negative relative to the top contact. The polarity of this induced field is the same as the polarity of the measured PC such that a negative OCP would drive the electrons to move from the bottom to the top contact in the external circuit, thus generating a negative PC. The polarities of the OCPs and PCs for eight molecular structures examined are summarized in Table 1, along with the DFT-predicted orbital energies and observed absorbance and PC peak energies. Note that in all cases the polarities of the OCP and PC match, and the peak absorbance photon energy is close to the maximum PC energy.

DOI: 10.1021/jacs.7b12577
J. Am. Chem. Soc. 2018, 140, 1900−1909

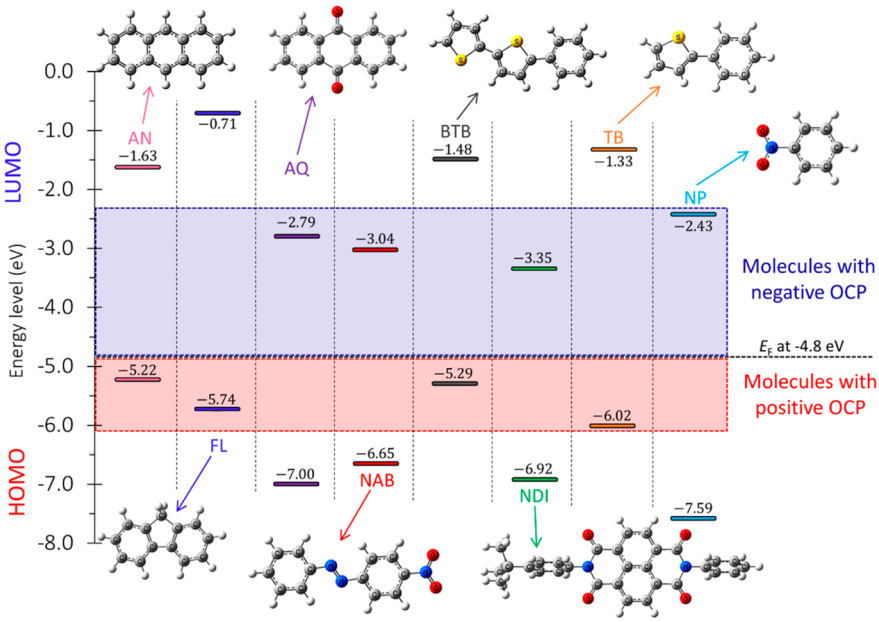

Figure 6. Correlation of the PC polarity and molecular orbitals. Frontier orbital energy diagram for the examined molecules relative to vacuum reference along with their Density Functional Theory (DFT) optimized molecular structure are shown. Orbital energies were calculated by DFT B3LYP 6-31G(d), in Gaussian 09. Fermi level of eC by UPS is −4.8 V vs vacuum.[41] Blue shading indicates molecules with negative PC and OCP, and red shading indicates molecules with positive PC and OCP. See Figures S5−S12 for visualization of the molecular orbitals and measured PC and phase shift for each molecule.

Control of the PC sign by the OCP was confirmed by application of an external bias during exposure to laser light, as shown in Figure 4d for the case of NAB. Under constant external bias, there is a reversible rise in the current upon exposure to the laser light which returns to the initial dark current if the optical shutter is closed. The PC at zero external bias is negative, and its magnitude can be increased with imposing external negative bias. However, a positive external bias decreases the PC and then cancels the PC when the bias equals +17 mV, which is equal and opposite to OCP observed without an external bias. Light absorption and photoinduced carrier generation still occur with the +17 mV bias applied, but there is no driving force for charge transport, and the carriers likely recombine. Applying a bias more positive than +17 mV reverses the polarity of the photoresponse to generate positive PC.

An additional probe of the PC mechanism is changing the direction of illumination, which is permitted by the symmetry of layer thicknesses and similar transparency of the top and bottom electrodes. Figure 5a shows photocurrent spectra for a BTB MJ, obtained similarly to that of Figure 4a, but stated as photocurrent magnitude rather than yield to avoid any ambiguity about polarity. Note that the PC does *not* change significantly when the MJ is illuminated through both the top and bottom contacts. The current and lock-in amplifier phase both indicate a positive photocurrent for either illumination geometry, with small differences due to focusing and contact transparency. Figure 5b shows the OCP for both top and back illumination with the 407 nm laser, also indicating no change in PC sign and minor differences in magnitude. For NAB devices, which exhibit negative PC and OCP with top illumination (Figure 4a and 4b), back illumination also resulted in negative PC and OCP for all wavelengths examined.

DISCUSSION

The collection of results for eight aromatic junction structures is summarized in Figure 4a. Table 1 indicates that the sign and wavelength maximum of the PC, as well as the absorption maximum of the molecular layer, all vary with molecular structure. In all cases for junctions with d > 5 nm, the PC spectrum is quite similar in shape to the UV−vis absorption spectrum for the molecular layer in contact with the eC electrodes. A starting point for understanding how molecular structure affects PC response is the DFT-determined frontier orbital energy levels, shown in Figure 6. A common proposal for molecular tunnel junctions is based on a tunneling barrier height equal to the difference in energy between the electrode Fermi energy and the frontier orbital of the molecule (HOMO or LUMO) closest in energy. The order in Table 1 is determined using this criterion, with AN having the smallest predicted barrier and NP having the largest for HOMO-mediated tunneling. As indicated by the fourth column of Table 1, AN, BTB, FL, and TB have smaller barriers for hole tunneling (ϕ_h), while NDI, NAB, AQ, and NP have smaller electron tunneling barriers (ϕ_e) based on their DFT energies. The eight molecules cover a wide range of the HOMO (−5.3 to −7.6 vs vacuum) and LUMO (−0.8 to −3.4) energy levels; hence, large variations in transport are expected based on this common model. A striking correlation is apparent in Figures 6 and 4a between the OCP and PC polarities and the frontier orbitals close to the Fermi level (E_F) of −4.8 V. Molecules with closer HOMO levels to E_F and smaller ϕ_h than ϕ_e (AN, BTB, FL, and TB) have positive OCP and PC, while those with closer LUMO levels and smaller φ_e (NDI, NAB, AQ, and NP) are negative. Although the free molecule DFT results are perturbed by electronic coupling with the contacts, they are consistent with the experiment in predicting whether the HOMO or LUMO energy is closest to the Fermi level. In addition, the predicted maximum absorption wavelength from

DOI: 10.1021/jacs.7b12577
J. Am. Chem. Soc. 2018, 140, 1900−1909

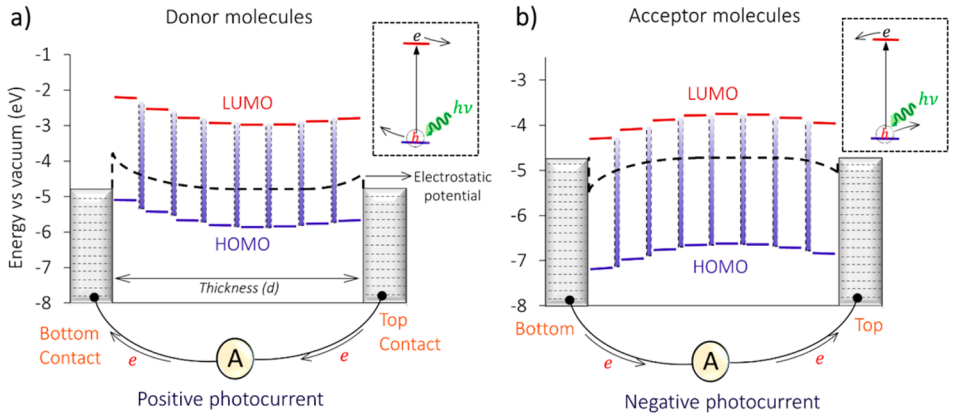

Figure 7. Schematic of the proposed mechanism for photocurrent production in thick molecular junctions. Energy level diagram at zero bias with eight pairs of localized HOMO (blue) and LUMO (red) orbitals for (a) AN junction as an example of a donor molecule with a smaller ϕ_h and (b) NDI junction as an example of an acceptor with a smaller ϕ_e. Dashed line within the molecule layer is the electrostatic potential profile resulting from partial charge transfer between the electrodes and the oligomeric molecule. Top corner inset of each panel shows the direction of charge separation upon absorption of light by the molecular layer.

TD-DFT is also close to the value observed experimentally in completed MJs. Similar sign selective currents have been reported for thermoelectric behavior in MJs;[25,42] however, the mechanism is much different for the PCs reported here. As discussed in detail in Supporting Information section 6, a thermoelectric response should be dependent on chopping frequency (not the case here) and should track optical power, contrary to the response shown in Figure 2a.

Regarding the origin of the PC, we can rule out the IPE mechanism observed for thinner MJs (d < 5 nm) in which the molecular absorption is weak.[34,35] The IPE mechanism involves optical excitation in the top contact and further transport to the bottom contact through the barrier determined by either HOMO or LUMO offset from the E_F. IPE provided a direct probe of the hole or electron barrier for direct tunneling when d < 5 nm, but was complicated when the molecule as well as the contact absorbed incident light.[34] In contrast, the current results for MJs with d > 5 nm clearly show that the PC is negligible for photon energies not absorbed by the molecular layer (Figures 3, 4a, and S5–S12). The PC spectra shapes and maxima for MJs with d > 5 nm differ significantly from those for IPE spectra reported previously (e.g., for AQ).[34]

The energy required for IPE is inherently smaller than the H–L gap, and the absence of PC for photon energies below the absorption onset of the molecular layer indicates that carriers excited in the contacts cannot traverse the thicker layers. Furthermore, the PC polarity and magnitude for the current MJs are the same when either the top or bottom electrode is illuminated (Figure 5), which is *not* consistent with the IPE mechanism. A critical observation is the strong correlation between the PC shape and the absorption spectrum of the molecular layer *as modified by electronic interactions with the contacts*. For each of the cases in Figure 3 and listed in Table 1, the onset and peak of the PC occur at similar wavelengths to those where molecular absorption occurs. As a consequence, the transport mechanism for the PC must involve the H–L gap, possibly by the photon-stimulated crossing of internal tunneling barriers, as discussed below.

We reported previously that bias-induced transport in carbon-based MJs (d > 5 nm) containing FL, AQ, BTB, and NAB, conductance correlated with the H–L gap rather than the offsets between E_F and either the HOMO or LUMO energies. We concluded that transport was by multistep tunneling through the H–L barrier in the interior of the MJ, and the smaller barriers at the electrode interfaces were not controlling the current.[6] We proposed that the tunneling barriers are likely located between the molecular subunits, where the electronic interactions between subunits of the molecular layer are weak and delocalization length is limited to one or at most two attached molecules. The direct correlation between optical absorption and PC implies that photon absorption permits carriers to traverse the H–L tunneling barrier and result in measurable PC under illumination. Similar to the conclusion from the transport study of the thick molecular layers[6] and in contrast to the IPE mechanism and direct tunneling transport,[35,36] transition from the H to L level in the bulk of the molecular component acts as a rate-limiting barrier for generating measurable PCs in the thick molecular layers studied here. Photon assistance is not dependent on the direction of illumination nor on optical absorption in the contacts, hence the direct correlation between absorption and PC.

While photon assistance of tunneling can explain the enhanced transport under illumination, it does not account for the polarity or driving force for charge transport. An important additional consideration is electronic coupling between the contacts and the molecules which causes local shifts in electrostatic potential due to partial charge transfer across the contact/molecule interface.[36,43−50] Since the current MJs are symmetric in terms of composition (i.e., Au/eC/oligomer/eC/Au) and the sign of the PC is independent of illumination direction, there must be asymmetry in the internal MJ structure or interfaces. The bottom eC/oligomer bond is covalent, while the top contact is presumably physisorbed, and the contact areas of the bottom and top electrodes are not likely to be identical. We propose that the electronic coupling at the bottom contact is stronger than at the top contact, resulting in greater broadening of the orbital energy levels and consequently greater partial charge transfer and energy shift at the bottom eC/oligomer interface. Figure 7 shows a schematic representation of an 8-unit oligomer between two contacts with a Fermi level at −4.8 V vs vacuum. The blue and red horizontal lines represent HOMO and LUMO energy levels, and the shaded regions between molecules represent

DOI: 10.1021/jacs.7b12577
J. Am. Chem. Soc. 2018, 140, 1900−1909

tunneling barriers. When the HOMO is closer to the electrode Fermi level than the LUMO (Figure 7a), there is charge transfer from the HOMO to the electrode, resulting in a positive shift of electrostatic potential and an upward shift in molecular energy levels near the electrode. Stronger electronic coupling at the bottom contact results in a larger shift, thus leading to the asymmetric potential profile shown as a dashed line in Figure 7a. As shown in Figure 7b, a LUMO closer to the Fermi level than the HOMO results in partial charge transfer into the oligomer and a downward shift in energy levels. The level shifts occur in the absence of illumination, and the asymmetry is a consequence of the difference in coupling strength at the two eC/oligomer interfaces. The shifts in electrostatic potential and orbital energy levels in the molecular layer near the contact/molecule interface caused by interface charge transfer is analogous to the well-known band bending concept in semiconductors.[51,52] The applicability of band bending to organic/metal interfaces has also been investigated and reviewed.[44,53] In addition, the concept of asymmetric coupling to the electrode was theoretically described by Galperin et al. to explain how optical pumping can create an internal driving force for charge flow in the molecular layer.[26,54,55]

When the MJ is illuminated at open circuit, charge flow across the H−L gaps is enabled, and electrons move down the potential profiles as shown in Figure 7. For electron donors (BTB, AN, FL, and TB), a deficit of electrons forms in the bottom contact, resulting in a positive OCP. For electron acceptors (NDI, AQ, NAB, and NP) the electron deficit occurs in the top electrode and the OCP is negative. For PC measurements the top and bottom electrodes are externally connected and optically pumped charges flow based on the internal potential gradient to produce a net charge flux and observable PC in the external circuit. The insets of Figure 7 show the direction of charge separation and flux for the donor and acceptor cases upon photon absorption in the molecular layer. The similarity of the molecular absorption spectra and the PC response implies that reorganization of the molecule does not occur significantly on the time scale of transport, as concluded previously for multistep tunneling under bias.[6] Although the specific photoinduced transitions and electron motions in ∼8 nm thick molecular junctions are complex and may involve multiple absorption, transport, and recombination events, the two important observations about OCP polarity and control of transport by the H−L gap are consistent with different coupling strengths at the electrodes and rate-limiting transport by sequential, photon-assisted tunneling across the H−L energy barrier. Further experiments measuring PC as a function of external bias and molecular layer thickness should elaborate additional mechanistic details and provide further insights about charge transport.

CONCLUSIONS

In summary, photocurrents observed in relatively thick carbon-based molecular junctions at zero bias provide useful diagnostics of junction behavior, notably the relationship between frontier orbital energies and device electronic behavior. First, the sign of the PC and open-circuit potential are clear and direct indications of whether the HOMO or LUMO are closer in energy to the electrode Fermi level. Second, the correlation of absorbance spectrum with PC indicates that the optical gap is the main factor controlling transport in thick junctions (d > 5 nm). Third, differences in electronic coupling at the top and bottom molecule/electrode interfaces are manifested as an observable OCP and PC polarity. Although asymmetric charge redistribution between the frontier molecular orbitals and the contacts is a prerequisite for the polarity of photovoltage, the rate-limiting step for observable PC is charge transfer within the molecular layer when the thickness becomes greater than is possible with single-step (direct) tunneling. This point is consistent with a previous conclusion of limited delocalization length within the molecular layer and H−L gaps as the effective barrier for the proposed multistep tunneling mechanism dominant in thick MJs (d > 5 nm).[6] We anticipate that both the IPE mechanism reported previously and the PCs induced by molecular absorption will continue to be useful probes of molecular junction energetics and electronic behavior.

METHODS

Device Fabrication and Characterization. Polished fused quartz chip (from Technical Glass Products, Inc.) were used as substrates in the current study to avoid the possibility of stray PC from a silicon substrate. A bottom contact consisting of 3 nm Cr, 20 nm Au and 10 nm of eC was deposited by electron beam assisted physical vapor deposition (Kurt Lesker PVD 75) through the physical shadow (See Supporting Information section 1 for full details). Molecular layers were grafted by electrochemical reduction of diazonium reagent on the surface of bottom contact. The thickness of the molecular layer was varied in the range of 5−12 nm by changing the range and number of voltammetric cycles, as shown in Figure S2 and Table S1. Finally, a top contact consisting of 10 nm eC and 15 nm of Au was deposited through the shadow mask with lines perpendicular to bottom contacts. An optical image of a complete chip is shown in Figure S4. The thickness of the deposited molecular layer was verified by AFM scratching technique described in Supporting Information (Figure S3). Current vs bias voltage (IV) curves were obtained in the four-wire mode as described previously.[41]

UV−vis Absorbance Spectroscopy. Polished fused quartz wafers were diced into 1.8 in 1.2 cm chips to serve as the substrate. Three nm of Cr, 20 nm of Au and 10 nm of eC was deposited as a blanket bottom contact (no lines). The optical absorbance of the chip was recorded using PerkinElmer Lambda 1050 dual beam spectrometer. Absorbance was references to the air and the samples were mounted perpendicular to the direction of the light beam. After obtaining a "substrate" absorption spectrum, the molecular layer was grafted by electrochemical reduction of diazonium reagents with the same procedure used for junction fabrication. The absorbance of resulting chip (bottom contact + molecular layer) was recorded. Finally, the absorbance measurement was repeated after deposition of top contact consisting of 10 nm of eC and 15 nm of Au.

AC Photocurrent Apparatus. A 150 W Xe Arc lamp (Newport model 6256) was used as a broad band light source. Monochromatic light with bandwidth of 13 nm was selected and transmitted through motorized Oriel Cornerstone monochromator model 74004. The output light was chopped at a frequency of ∼405 Hz and then focused on the junction by a series of lenses. The illuminated molecular junction was connected via tungsten probe and BNC cables to the AC input of a dual phase lock-in amplifier (LIA, Stanford Research-830). The positive input terminal was always connected to the bottom contact. A custom LabView data acquisition program controlled the output wavelength of the monochromator and recorded the output current and phase from the lock-in amplifier. The light intensity of selected wavelength was measured by Newport power meter (Model 1936-R) at the sample. The phase calibration was done by the photodiode with the known sign of photocurrent and zero phase shift. While the sign, shape and maximum wavelengths of the PC spectrum were consistent for all samples of a given molecule (listed in Table S1), the PC intensity varied with layer thickness.

OCP and Photocurrent Measurements under Bias. A Thorlabs 407 nm laser diode powered by a Thorlabs LDC 210C

DOI: 10.1021/jacs.7b12577
J. Am. Chem. Soc. 2018, 140, 1900−1909

controller and TED 200C thermoelectric temperature controller was used as a source of illumination. The light intensity of the laser beam at the sample was determined using a Newport power-meter directly above the sample. The junction's bottom and top contact were connected to the input of a Keithley 6517 picoammeter using tungsten probes and BNC cables. Exposure time was controlled with a Thorlabs Ø1 optical beam shutter. The shutter was triggered by the voltage output of the Keithley 6517, and a visual basic program collected the current or voltage data output while also controlling the shutter. In case of PC measurement under bias, a source-measurement unit (Keithley 2602B) was used in series for applying the external bias across the junction under computer control. Instrument schematics and details are provided in Supporting Information.

■ ASSOCIATED CONTENT

Supporting Information

The Supporting Information is available free of charge on the ACS Publications website at DOI: 10.1021/jacs.7b12577.

Supplementary methods; equations used for yield calculation; photocurrent, phase shift and absorption of examined molecules; *IV* curves and photocurrent as a function of thicknesses of anthraquinone and fluorene; statistics for multiple samples of each molecular structure; thermoelectric effect discussion; apparatus schematics of photocurrent under bias measurement (PDF)

■ AUTHOR INFORMATION

Corresponding Author

*richard.mccreery@ualberta.ca

ORCID

Amin Morteza Najarian: 0000-0002-0455-0451

Richard L. McCreery: 0000-0002-1320-4331

Notes

The authors declare no competing financial interest.

■ ACKNOWLEDGMENTS

This work was supported by the University of Alberta, the National Research Council of Canada, the National Sciences and Engineering Research Council, and Alberta Innovates. The authors thank Colin Van Dyck and Adam Bergren for useful conversations and suggestions, and Prof. Jean-Christophe Lacroix at the University of Paris for providing the BTB amine precursor.

■ REFERENCES

(1) Xiang, D.; Wang, X.; Jia, C.; Lee, T.; Guo, X. *Chem. Rev.* **2016**, *116*, 4318−4440.

(2) Vilan, A.; Aswal, D.; Cahen, D. *Chem. Rev.* **2017**, *117*, 4248−4286.

(3) Aradhya, S. V.; Venkataraman, L. *Nat. Nanotechnol.* **2013**, *8*, 399−410.

(4) Su, T. A.; Neupane, M.; Steigerwald, M. L.; Venkataraman, L.; Nuckolls, C. *Nature Rev. Mater.* **2016**, *1*, 16002.

(5) Jeong, H.; Kim, D.; Xiang, D.; Lee, T. *ACS Nano* **2017**, *11*, 6511−6548.

(6) Morteza Najarian, A.; McCreery, R. L. *ACS Nano* **2017**, *11*, 3542−3552.

(7) Sangeeth, C. S. S.; Demissie, A. T.; Yuan, L.; Wang, T.; Frisbie, C. D.; Nijhuis, C. A. *J. Am. Chem. Soc.* **2016**, *138*, 7305−7314.

(8) Bayat, A.; Lacroix, J.-C.; McCreery, R. L. *J. Am. Chem. Soc.* **2016**, *138*, 12287−12296.

(9) Trasobares, J.; Vuillaume, D.; Theron, D.; Clement, N. *Nat. Commun.* **2016**, *7*, 12850.

(10) Chabinyc, M. L.; Chen, X.; Holmlin, R.; Jacobs, H.; Skulason, H.; Frisbie, C. D.; Mujica, V.; Ratner, M.; Rampi, M. A.; Whitesides, G. M. *J. Am. Chem. Soc.* **2002**, *124*, 11730−11736.

(11) Yuan, L.; Nerngchamnong, N.; Cao, L.; Hamoudi, H.; del Barco, E.; Roemer, M.; Sriramula, R. K.; Thompson, D.; Nijhuis, C. A. *Nat. Commun.* **2015**, *6*, 6324.

(12) Li, Z.; Li, H.; Chen, S.; Froehlich, T.; Yi, C.; Schonenberger, C.; Calame, M.; Decurtins, S.; Liu, S. X.; Borguet, E. *J. Am. Chem. Soc.* **2014**, *136*, 8867−70.

(13) Min, M.; Seo, S.; Lee, S. M.; Lee, H. *Adv. Mater.* **2013**, *25*, 7045−50.

(14) Green, J. E.; Choi, J. W.; Boukai, A.; Bunimovich, Y.; Johnston-Halperin, E.; DeIonno, E.; Luo, Y.; Sheriff, B. A.; Xu, K.; Shin, Y. S.; Tseng, H. R.; Stoddart, J. F.; Heath, J. R. *Nature* **2007**, *445*, 414−7.

(15) Whalley, A. C.; Steigerwald, M. L.; Guo, X.; Nuckolls, C. *J. Am. Chem. Soc.* **2007**, *129*, 12590−12591.

(16) Jia, C.; Migliore, A.; Xin, N.; Huang, S.; Wang, J.; Yang, Q.; Wang, S.; Chen, H.; Wang, D.; Feng, B.; Liu, Z.; Zhang, G.; Qu, D.-H.; Tian, H.; Ratner, M. A.; Xu, H. Q.; Nitzan, A.; Guo, X. *Science* **2016**, *352*, 1443−1445.

(17) Schwarz, F.; Kastlunger, G.; Lissel, F.; Egler-Lucas, C.; Semenov, S. N.; Venkatesan, K.; Berke, H.; Stadler, R.; Lortscher, E. *Nat. Nanotechnol.* **2016**, *11*, 170−6.

(18) Wagner, S.; Kisslinger, F.; Ballmann, S.; Schramm, F.; Chandrasekar, R.; Bodenstein, T.; Fuhr, O.; Secker, D.; Fink, K.; Ruben, M.; Weber, H. B. *Nat. Nanotechnol.* **2013**, *8*, 575−9.

(19) Du, W.; Wang, T.; Chu, H.-S.; Wu, L.; Liu, R.; Sun, S.; Phua, W. K.; Wang, L.; Tomczak, N.; Nijhuis, C. A. *Nat. Photonics* **2016**, *10*, 274−280.

(20) Conklin, D.; Nanayakkara, S.; Park, T. H.; Lagadec, M. F.; Stecher, J. T.; Chen, X.; Therien, M. J.; Bonnell, D. *ACS Nano* **2013**, *7*, 4479−4486.

(21) Wang, T.; Nijhuis, C. A. *Appl. Mater. Today* **2016**, *3*, 73−86.

(22) Pourhossein, P.; Vijayaraghavan, R. K.; Meskers, S. C. J.; Chiechi, R. C. *Nat. Commun.* **2016**, *7*, 11749.

(23) Ivashenko, O.; Bergren, A. J.; McCreery, R. L. *Adv. Electr. Mater.* **2016**, *2*, 1600351.

(24) Evangeli, C.; Gillemot, K.; Leary, E.; Gonzalez, M. T.; Rubio-Bollinger, G.; Lambert, C. J.; Agrait, N. *Nano Lett.* **2013**, *13*, 2141−5.

(25) Widawsky, J. R.; Darancet, P.; Neaton, J. B.; Venkataraman, L. *Nano Lett.* **2012**, *12*, 354−8.

(26) Galperin, M.; Nitzan, A. *Phys. Chem. Chem. Phys.* **2012**, *14*, 9421−9438.

(27) Afanasev, V. V. *Internal Photoemission Spectroscopy: Principles and Applications*; Elsevier Science: Oxford, U.K., 2008.

(28) Wang, F.; Melosh, N. A. *Nat. Commun.* **2013**, *4*, 1711.

(29) Afanas'ev, V. V. *sciencedirect* **2014**, 109−160.

(30) Goodman, A. M. *J. Appl. Phys.* **1970**, *41*, 2176−2179.

(31) Powell, R. *J. Appl. Phys.* **1970**, *41*, 2424.

(32) Gundlach, K. *J. Appl. Phys.* **1975**, *46*, 5286.

(33) Loo, Y.-L.; Lang, D. V.; Rogers, J. A.; Hsu, J. W. P. *Nano Lett.* **2003**, *3*, 913−917.

(34) Fereiro, J. A.; Kondratenko, M.; Bergren, A. J.; McCreery, R. L. *J. Am. Chem. Soc.* **2015**, *137*, 1296−1304.

(35) Fereiro, J. A.; McCreery, R. L.; Bergren, A. J. *J. Am. Chem. Soc.* **2013**, *135*, 9584−9587.

(36) Sayed, S. Y.; Fereiro, J. A.; Yan, H.; McCreery, R. L.; Bergren, A. J. *Proc. Natl. Acad. Sci. U. S. A.* **2012**, *109*, 11498−11503.

(37) Yoon, H. J.; Bowers, C. M.; Baghbanzadeh, M.; Whitesides, G. M. *J. Am. Chem. Soc.* **2014**, *136*, 16−19.

(38) Yoon, H. J.; Shapiro, N. D.; Park, K. M.; Thuo, M. M.; Soh, S.; Whitesides, G. M. *Angew. Chem., Int. Ed.* **2012**, *51*, 4658−4661.

(39) Choi, S. H.; Kim, B.; Frisbie, C. D. *Science* **2008**, *320*, 1482−1486.

(40) Amdursky, N.; Marchak, D.; Sepunaru, L.; Pecht, I.; Sheves, M.; Cahen, D. *Adv. Mater.* **2014**, *26*, 7142−7161.

(41) Morteza Najarian, A.; Szeto, B.; Tefashe, U. M.; McCreery, R. L. *ACS Nano* **2016**, *10*, 8918−8928.

DOI: 10.1021/jacs.7b12577
J. Am. Chem. Soc. 2018, 140, 1900−1909

(42) Reddy, P.; Jang, S.-Y.; Segalman, R. A.; Majumdar, A. *Science* **2007**, *315*, 1568−1571.
(43) Zotti, G.; Zecchin, S.; Schiavon, G.; Louwet, F.; Groenendaal, L.; Crispin, X.; Osikowicz, W.; Salaneck, W.; Fahlman, M. *Macromolecules* **2003**, *36*, 3337−3344.
(44) Hwang, J.; Wan, A.; Kahn, A. *Mater. Sci. Eng., R* **2009**, *64*, 1−31.
(45) Vilan, A.; Yaffe, O.; Biller, A.; Salomon, A.; Kahn, A.; Cahen, D. *Adv. Mater.* **2010**, *22*, 140−159.
(46) Van Dyck, C.; Ratner, M. A. *J. Phys. Chem. C* **2017**, *121*, 3013−3024.
(47) Van Dyck, C.; Geskin, V.; Cornil, J. *Adv. Funct. Mater.* **2014**, *24*, 6154−6165.
(48) Xie, Z.; Bâldea, I.; Smith, C. E.; Wu, Y.; Frisbie, C. D. *ACS Nano* **2015**, *9*, 8022−8036.
(49) Kim, B.; Choi, S. H.; Zhu, X. Y.; Frisbie, C. D. *J. Am. Chem. Soc.* **2011**, *133*, 19864−19877.
(50) Zheng, Y. J.; Huang, Y. L.; Chen, Y.; Zhao, W.; Eda, G.; Spataru, C. D.; Zhang, W.; Chang, Y. H.; Li, L. J.; Chi, D.; Quek, S. Y.; Wee, A. T. *ACS Nano* **2016**, *10*, 2476−84.
(51) Zhang, Z.; Yates, J. T. *Chem. Rev.* **2012**, *112*, 5520−5551.
(52) Hagfeldt, A.; Graetzel, M. *Chem. Rev.* **1995**, *95*, 49−68.
(53) Ishii, H.; Sugiyama, K.; Ito, E.; Seki, K. *Adv. Mater.* **1999**, *11*, 605−625.
(54) Galperin, M.; Nitzan, A. *Phys. Rev. Lett.* **2005**, *95*, 206802.
(55) Galperin, M.; Nitzan, A.; Ratner, M. A.; Stewart, D. R. *J. Phys. Chem. B* **2005**, *109*, 8519−8522.

DOI: 10.1021/jacs.7b12577
J. Am. Chem. Soc. 2018, 140, 1900−1909